Engineering Fracture Mechanics 104 (2013) 56–79

Contents lists available at SciVerse ScienceDirect

Engineering Fracture Mechanics

journal homepage: www.elsevier.com/locate/engfracmech

Identification of mode-I cohesive parameters for bonded interfaces based on DCB test

Nunziante Valoroso [a,*], Salvatore Sessa [b], Marcello Lepore [c], Gabriele Cricrì [c]

[a] Dipartimento per le Tecnologie, Università di Napoli Parthenope, Centro Direzionale Isola C4, 80143 Napoli, Italy
[b] Dipartimento di Ingegneria Strutturale, Politecnico di Milano, Piazza Leonardo da Vinci 12, 20133 Milano, Italy
[c] Dipartimento di Ingegneria Industriale, Università di Salerno, via Ponte Don Melillo 1, 84084 Fisciano, Italy

ARTICLE INFO

Article history:
Received 3 April 2012
Received in revised form 23 November 2012
Accepted 11 February 2013
Available online 27 March 2013

Keywords:
Cohesive-zone models
Parameter identification
Adhesive joints
Double cantilever beam
Mode-I fracture
Test protocol

ABSTRACT

An inverse procedure is developed for computing the material parameters of the class of intrinsic cohesive-zone models for the analysis of structural adhesive joints presented in [Valoroso N, Champaney L. A damage-mechanics-based approach for modeling decohesion in adhesively bonded assemblies, Engng Fract Mech 2006;73:2774–801.]. In particular, using the same experimental data recorded as of ISO 25217 test protocol and Double Cantilever Beam bonded specimens, a deterministic identification that overcomes the usual limitations and difficulties of ISO 25217 is proposed to estimate the mode-I cohesive parameters. The driving rationale for our approach to identification is to set up an inverse procedure based on one single experimental test that uses the measured load–deflection curve and crack length as data set. A finite element model updating scheme is used that renders extensions to more general situations such as different geometries, large displacements and nonlinearities in the bulk material, possible with minor modifications. Experiments are conducted for symmetric DCB specimens under pure mode-I bending and an optimization problem is solved to find a suitable agreement between experimental data and finite element computations. Identification results are presented and the key role played by the crack progression in the identification is discussed to assess the effectiveness of the proposed approach.

1. Introduction

In recent years use of structural adhesives has become widespread owing to their many inherent desirable features with respect to more traditional welded or mechanical fastening systems [1]. For adhesive joints to be safely included in structural applications the ability to predict joint damage is of utmost importance. This is in general not achievable using strength-based approaches because of the high stress concentrations occurring at bi-material interfaces or at the tip of pre-existing flaws that often serve as initiation sites for de-cohesion and macro cracks.

A number of quite general models have been presented in the literature that describe the Mechanics of adhesion and adhesive joints. On the one hand, starting from the consideration of an interphase, basic elastic models [2] and more refined ones incorporating friction and contact [3], isotropic elastic–plastic damage [4], possibly non-isotropic behavior [5], and residual stresses [6] have been obtained via the asymptotic expansion method introducing scalings through a small pertur-

* Corresponding author. Tel.: +39 081 5476720; fax +39 081 5476777.
E-mail addresses: nunziante.valoroso@uniparthenope.it (N. Valoroso), sal.sessa@gmail.com (S. Sessa), malepore@unisa.it (M. Lepore), gcricri@unisa.it (G. Cricrì).
URL: http://www.dit.uniparthenope.it (N. Valoroso).

0013-7944/$ - see front matter © 2013 Elsevier Ltd. All rights reserved.
http://dx.doi.org/10.1016/j.engfracmech.2013.02.008

Nomenclature

a_0	total crack length of the DCB (initial value)
a	total crack length of the DCB (current value)
a_i^{comp}	crack length computed via the FE model (scalar) at time τ_i
b	specimen width
h	thickness of the DCB arms
h_1	thickness of the adhesive layer
k, k^-	interface stiffness in tension or compression
l_2	half length of the loading block of the DCB
l_3	length of the loading block of the DCB
l_c	characteristic length parameter
n	compliance exponent in Experimental Compliance Method (ECM)
n_τ, m_τ	number of measurements stations
t	interface (normal) traction
t_{max}	mode-I cohesive strength
$[\![u]\!]$	displacement jump
C	specimen compliance
C_w	specimen compliance (Winkler-type beam model)
D	damage variable
E	elastic modulus of the bulk material
F	large displacements correction factor
F_A	damage function
H	height of the loading block of the DCB
G	energy release rate
G_w	energy release rate (Winkler-type beam model)
G_{Ic}	mode-I fracture energy
$\overline{G}_{Ic,(i)}$	average mode-I fracture energy at time τ_i
K_{tan}	interface tangent stiffness
N	load-block factor
P	reaction force at each arm of the DCB
P_i^{comp}	reaction force computed via the FE model (scalar) at time τ_i
U	stored elastic energy
Y, Y^*	damage-driving force and its threshold value
$\boldsymbol{x}$	material parameters to be identified (vector)
$\hat{\boldsymbol{x}}$	material parameters at solution (vector)
$\mathbf{a}^{comp}$, a^{comp}	crack lengths computed via the FE model (vector and scalar)
$\mathbf{a}^{meas}$	measured crack lengths (vector)
$\mathbf{R}_P$, $\mathbf{R}_a$	residual vectors
$\boldsymbol{P}^{meas}$	measured reaction forces (vector)
$\boldsymbol{P}^{comp}$, P^{comp}	reaction forces computed via the FE model (vector and scalar)
α_P, α_a	weighting coefficients of the cost function
δ	relative end displacement of the DCB
δ_i	relative end displacement at time τ_i
λ	characteristic length of Winkler-type beam model
σ	generic time instant
τ,τ_i	time stations
ϕ	damage criterion
$\omega(\boldsymbol{x})$	cost (objective) function for the identification problem
Δ	additional crack length in Corrected Beam Theory (CBT)
$\Phi(\tau_i)$	energy dissipated up to time τ_i

bation parameter. On the other side, within the setting of a phenomenological approach are worth mentioning the work of Frémond [7] and its later extensions provided in [8–10] among others. Key features here are the consideration of interfaces as material surfaces and use of the concept of intensity of adhesion in the form of a complementary damage variable quantifying surface attraction in the sense of classical theories of adhesion, see e.g. [11,12].

In the same context one can categorize the widely used cohesive-zone models (CZMs) originating from those proposed by Dugdale [13] and Barenblatt [14]. Since initially motivated by the need to characterize the stress state near equilibrium cracks, in CZMs one generally speaks of damage rather than adhesion. However, the underpinning concept remains the same, i.e. that fracture is a progressive phenomenon in which separation takes place across an extended crack tip, the so-termed process zone, and is resisted by attractive (cohesive) forces. The CZM approach has become very popular and an increasing

number of contributions have appeared in the literature in the last 15 years, see e.g. [15,16] for recent overviews. This is due to the intrinsic flexibility and easy-to-implement treatment of fracture via the CZM concept, whereby a link between microstructural failure mechanisms and the continuum deformation field is established by incorporating fracture parameters into the material description. Such parameters are typically the cohesive strength and the fracture energy (toughness) and should be obtainable from experiments in order to calibrate the constitutive laws that are being used for predictive computations.

For adhesively bonded specimens the international standard for the determination of mode-I fracture energy G_{Ic} is ISO 25217 [17]. This is the outcome of an international Round Robin test program organized by the ESIS Technical Committee 4 whose results are summarized in [18]. In particular, the analysis methods suggested in ISO 25217 concern the Double Cantilever Beam (DCB) geometry and basically rely upon the Linear Elastic Fracture Mechanics (LEFM) argument. To this end use is made either of a beam theory approach [19,20] or of an experimental compliance calibration method [21], which both require the simultaneous recording during the experiment of the total load P, the relative end displacement δ between the arms of the DCB, and the crack length a. Using this data set the standard approach allows for the determination of G_{Ic} and also for data cross-checking, e.g. by determining the elastic modulus in bending and the resistance curve (R-curve), which should both exhibit little dependence from the extension of the crack at least in the stable propagation phase.

Data reduction as suggested in ISO 25217 can be readily carried out using the Excel spreadsheet available to this scope from the Imperial College at http://www3.imperial.ac.uk/meadhesion/testprotocols/lefm. Interpretation of results can however be not straightforward despite the apparent simplicity of the analysis. Actually, in many cases the hypotheses underlying the procedures described in ISO 25217 may be not strictly satisfied. This typically occurs whenever soft adhesives are used, whereby a contribution of the adhesive compliance to the deformation of the tested specimens is present from the very beginning of the test. Moreover, difficulties may also arise for experimental load–deflection curves exhibiting instabilities during crack propagation, or if non-negligible R-curve effects are present. In such and other cases use of the basic LEFM argument to identify the adhesive fracture parameters is probably not the best choice.

As an example, in Figs. 1 and 2 are reported in normalized form the experimental load–deflection curves obtained for the series of four symmetric DCB specimens that are considered in this study. In the same figures are also depicted the elastic loading lines of a DCB with the same geometric and mechanical properties and initial fracture lengths $a = 40$ mm and $a = 45$ mm respectively, i.e. two ideal LEFM responses before any fracture propagation occurs. Simple inspection on these plots reveals that the experimental curves exhibit a greater compliance with respect to the elastic ones. One may therefore argue that the LEFM approach is not fully adequate to model these experiments because there is a non-negligible contribution of cohesive tractions ahead of the crack tip to the deformation of the system, which in turn implies that small scale yielding conditions do not hold.

In order to approximately quantify this effect, at least for the initial loading phase before crack propagation, a simple schematization of the DCB via a conventional Euler–Bernoulli beam on a Winkler-type elastic foundation suffices. In particular, as shown later on in the paper, if the interface properties are known, use of a spring constant nearly equal to the interface elastic stiffness allows to well represent the initial experimental compliance of the tested samples. As shown in [22], the approach based on the beam on elastic foundation has the advantage that many corrections introduced in modified beam theories (usually in the form of an additional crack length) can be avoided, see in this respect also [23,24]. This is undoubtedly interesting in view of identification of the fracture energy since the resulting model used for the DCB is fully analytical. However, the elastic foundation model requires the stiffness of the adhesive layer as an additional input parameter that has to be determined independently from the fracture energy for the method to be successfully used.

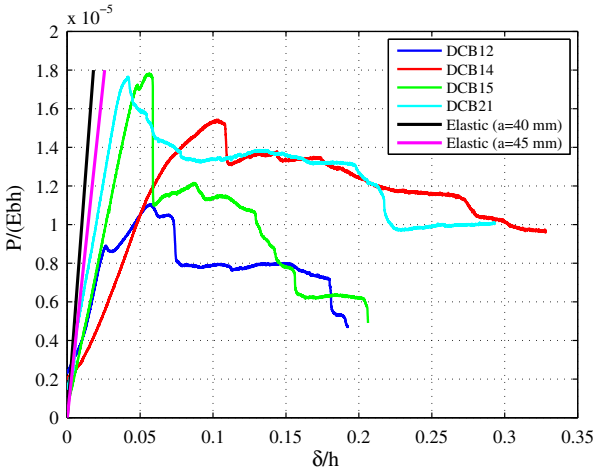

Fig. 1. Normalized load–deflection curves for some representative tested DCB samples. Solid black and magenta lines represent ideally linear elastic solutions.

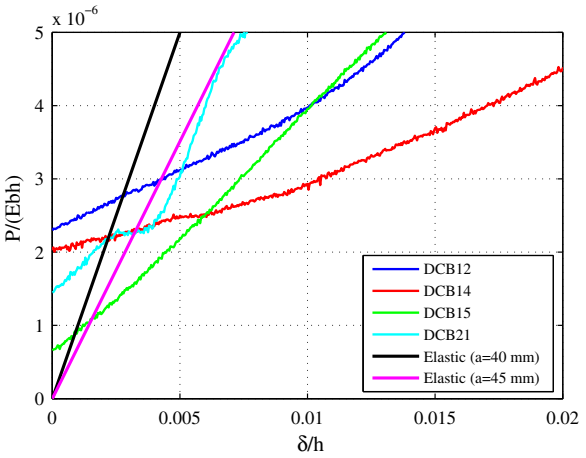

Fig. 2. Normalized load–deflection curves for some representative tested DCB samples and ideally linear elastic solutions. Enlarged view at origin.

In the present context the significant role played by cohesive forces can also be recognized by appealing to the definition of characteristic length parameter [25]:

$$l_c = \frac{E\, G_{Ic}}{t_{max}^2} \tag{1}$$

E being the elastic modulus of the bulk material and t_{max} the cohesive strength of the adhesive layer. The above length parameter is an inverse measure of material brittleness, i.e. the smaller l_c the more brittle the material; as such, it provides an approximate measure of the length over which the cohesive zone plays a role [26]. Actually, one could check a posteriori that in order to consider the LEFM approach well suited for the case at hand the characteristic length parameter (1) should be significantly smaller compared to all dimensions of the structure, see also [27] for a more comprehensive discussion.

Motivated by the intrinsic limitations of LEFM-based methods, a number of studies have been presented covering the identification of adhesive fracture parameters based on CZMs. Focusing our interest on mode-I parameters and the classical DCB specimen subject to end forces, are worth mentioning the works of Tamuzs et al. [28] and of de Moura et al. [29]. In both papers use is made of compliance-based methods in which crack length measurements are not directly used to limit errors due to ambiguities in the definition of the crack tip.

In particular, in [28] the shape of the cohesive relationship is not defined a priori and the tractions over the crack faces are computed by differentiating the energy release rate with respect to the end-opening of the bonded region as first suggested in [30]. This methodology has much in common with methods that use the J-integral approach to solve the problem, see e.g. [31–35] among others, in that the cohesive zone properties are obtained via numerical differentiation of the J-integral. As explicitly noted in [31], this can however produce significant errors for measurements that are not accurate enough.

On the contrary, in the procedure adopted in [29] the mode I toughness G_{Ic} is estimated using the compliance of the DCB; the remaining parameters that characterize a prescribed shape of the cohesive relationship are then computed using an optimization procedure to enforce agreement between numerical and experimental load–deflection curves. In a sense a generalization of this last approach is represented by the recent work of Gustafson and Waas [36]. Based on a pseudo-experimental data set, a sensitivity analysys and a statistical synthesis of different tests are carried out therein to obtain a complete set of material parameters for bonded structures taking into account interactions between different coupon-level experiments (including the DCB). Different from the previous paper, where classical data reduction schemes are envisaged, Valoroso and Fedele [37] used either kinematic data (surface displacements of a suitable region-of-interest), global static data (the load–deflection response), or a combination of the two to provide the data set of the DCB. Moreover, they computed parameter sensitivities via the direct differentiation method (DDM) and show important qualitative features of the DCB test that are quite useful when dealing with data originating from full-field measurements [38].

Apart from these differences, the last two papers put forward an important common opinion, i.e. that identification is not only interesting from a fundamental standpoint, in which case it would be preferable not to make a priori assumptions on the shape of the traction–separation law, but mainly for the calibration of a constitutive law to be used in predictive computations. One drawback of a priori assumed shapes of the cohesive law is the fact that, to a certain extent, it introduces a constraint. This is however balanced by the fact that analytical expressions are more suitable for finite element calculations, which do not require only function evaluations but also linearizations for computing, e.g. the material tangent matrix and also for carrying out the sensitivity analyses. Moreover, in order to obtain an experimental procedure that could be widely applicable, in the Authors' opinion one should try avoiding quite specific testing devices (e.g. to apply bending moments to the DCB specimen) and/or very particular measurements (e.g. for obtaining the elongation of the adhesive layer) and possibly use only a universal testing device to carry out the usual DCB test under displacement control.

With this motivation, in this paper we develop an analysis that differs from the aforementioned ones based either on beam theories, compliance calibration or J-integral related methods and use the same data set (P,δ,a) as in LEFM-based methods to get out from one single test the two mode-I parameters, i.e. the strength and toughness, of the cohesive model contributed by the first Author in [39]. In particular, an inverse methodology is developed that is able to determine the material parameters as the solution of a nonlinear programming problem. One of our purposes is to try keeping a general coherence between the data reduction scheme and the finite element model in which the identified cohesive law is being later used. To this end a least-squares norm is used as objective function that quantifies the distance between experimental data and the analogous quantities computed via finite elements as a function of the unknown parameters. The optimization problem is solved using either a zero-order method (constrained simplex) or a first-order gradient-based algorithm. In this last case the exact algorithm linearization requires the computation of the sensitivities of the finite element solution vector based on DDM.

The data set for the identification process is provided by the usual measurements (P,δ,a) recorded during the experimental tests on symmetric DCB specimen in pure mode-I bending. It is shown that, unlike most classical data reduction schemes [18], in the proposed identification procedure the same data set as described in ISO 25217 allows to obtain the two model parameters that fully characterize the mode-I response of the cohesive model. This is achieved by defining the cost function to be minimized in a way to explicitly account for crack progression, a datum that is directly related to the position of the process zone along the interface and, hence, to the global amount of energy consumed during the experiment. It bears emphasis that for our purposes the exact position of the crack tip is not strictly needed and a conventional amount of opening displacement can be taken as a reference in order to follow the crack advancement.

The numerical results presented in the paper show that whenever such quantity is explicitly used, a better accuracy is achieved in the identification. This fact is also strengthened by comparisons with a model of beam on elastic foundation as well as by the observation that, as shown in the paper in graphical form, inclusion of a term related to global energy dissipation in the cost function produces a convexification of the function itself with respect to the stiffness parameter. Therefore, an easier minimization (and identification) is achieved.

The outline of the paper is as follows.

In Section 2 is given a concise description of the DCB test and of the different methods of analysis. The adopted materials and the procedure followed for sample preparation and data reduction according to ISO 25217 are then presented in Section 3. The cohesive damage model for the one-dimensional mode-I case is described in section 4 and the identification procedure is detailed in Section 5. Results and discussion are presented in Section 6 that enlighten the distinctive features of the proposed procedure. Conclusions and future research prospects are finally outlined in Section 7.

2. Background: the DCB test

The symmetric DCB is the standard test specimen used for obtaining the mode-I adhesive fracture energy G_{Ic} of bonded joints. Since the bond layer is typically thin and weaker than adherends, in this test the adhesive is highly constrained and through-the-thickness deformation is usually neglected. Data reduction schemes suggested in test standards, see e.g. ISO 25217 [17], make use of methods based upon LEFM and require the values of total load P, end relative displacement δ and crack length a to be recorded during the test. Restricting attention to the case in which the DCB arms are linearly elastic, the energy release rate is found using the Irwin–Kies relationship ([40]):

$$G = \frac{1}{b}\frac{\partial U}{\partial a} = \frac{P^2}{2b}\frac{\partial C}{\partial a} \tag{2}$$

where U is the elastic energy stored in the structure, b is the specimen width and $C = \delta/P$ its compliance.

Basically, the different reduction methods differ on how the compliance C in expression (2) is computed and differentiated. However, in most of these methods the crack length a has to be measured, which in general is not straightforward because the process zone can develop over a length more or less extended depending upon the toughness and strength of the adhesive. This may render the crack tip difficult to be located within the desired precision. Moreover, factors such as transverse shear, adhesive compliance and crack tip deformation, beam shortening and possible specimen stiffening caused by load blocks bonded to the DCB arms require the introduction of corrective terms in the expression of the compliance in the form of an additional crack length Δ, a load-block factor N and a large displacements correction F.

In particular, in Corrected Beam Theory (CBT) analysis [19,20] the energy release rate is computed as:

$$G = G(P,\delta,a,\Delta) = \frac{3P\delta}{2b(a+\Delta)}\cdot\frac{F}{N} \tag{3}$$

The average crack length correction Δ in (3) is obtained as the intercept with the negative a axis of a straight line computed from a linear regression on the cube root of the compliance expressed in the form:

$$\frac{C}{N} = \frac{8}{Ebh^3}\cdot(a+\Delta)^3 \tag{4}$$

E being the elastic modulus and h the thickness of the arms of the DCB.

A different approach is the one used in Experimental Compliance Method (ECM) initially proposed in [21], whereby the energy release rate is directly determined using (2) in the form:

$$G = G(P, \delta, a, n) = \frac{nP\delta}{2ba} \cdot \frac{F}{N} \tag{5}$$

Application of the above relationship requires knowledge of the coefficient n that is used for curve fitting the global specimen compliance according to Berry's methodology ([21]):

$$\frac{C}{N} = ka^n \tag{6}$$

In particular, the exponent n is determined experimentally as the slope of a straight line adjusted on the experimental values plotted in terms of log (C/N) vs log (a). It has to be kept in mind that the above recalled data reduction schemes possess an intrinsic weakness due to the fact that they require an accurate monitoring of the crack during its progression. This may not be easy to perform since unstable crack propagation and/or wide process zones may prevent from a sufficiently accurate identification of the crack tip and, hence, lead to erroneous estimates of the crack length a. On the other hand, use of expressions (3) and (5) seems to be somehow self-contradictory in the framework of a LEFM approach since for the DCB the fracture energy G_{Ic} is, at least theoretically, independent from the crack length a in the propagation phase. These expressions have indeed the only scope of allowing data cross-checking since, according to the ISO protocol, in order to consider the results of the experimental tests acceptable one should verify that there is very little or no R-curve effect at all at least during stable crack propagation.

As shown in [28], an effective synthesis of the two above discussed methods for data reduction can be obtained by eliminating the crack extension from (3) so to express this relationship in terms of compliance as it was in (2) before computing the derivative. In particular, neglecting all corrective terms F, N, Δ and using the definition of the compliance $C = \delta/P$, one can eliminate the crack length a from (3) and (4) to get:

$$G = G(P, \delta) = \frac{12P^2}{Eb^2h^3} \cdot \left(\frac{Ebh^3\delta}{8P}\right)^{\frac{2}{3}} \tag{7}$$

Relationship (7) is the one used in the so-called Modified Compliance Calibration Method (MCCM) [41] and is known to perform much better than both CBT and ECM since it implicitly accounts for all necessary corrections to the compliance of an ideal cantilever beam through the experimental values of the load P and deflection δ. For comparison purposes, in the following we shall compute the mode-I fracture energy from the experimental data using all the reduction methods described in the present section. The R-curves will be however provided only for CBT and ECM and not for the MCCM since relationship (7) contains no explicit dependence from the crack extension a.

For soft adhesive layers, accurate estimates for the fracture energy can be obtained by incorporating interface elasticity into the model via the Winkler-type elastic foundation. Actually, in such cases the process zone could be quite extended, whereby errors may occur in the evaluation of G_{Ic} [42]. In particular, using the 1D Euler–Bernoulli theory and Winkler-type distributed springs to model the adhesive layer, the compliance and the energy release rate of the symmetric DCB are respectively obtained as [43]:

$$C_w = \frac{\delta}{P} = \frac{8a^3}{Ebh^3} \cdot \frac{3 + 6\lambda a + 6(\lambda a)^2 + 2(\lambda a)^3}{2(\lambda a)^3} \tag{8}$$

$$G_w = \frac{P^2}{2b}\frac{\partial C_w}{\partial a} = \frac{12P^2(\lambda a + 1)^2}{\lambda Eb^2h^3} \tag{9}$$

where

$$\lambda = \left(\frac{k}{3Eh^3}\right)^{\frac{1}{4}} \tag{10}$$

is the inverse characteristic length of the model that depends on the elastic stiffness of the interface k. Manifestly, use of (8) and (9) require that the interface stiffness k be known in advance. Hence, the above relationships could be used to verify a posteriori the results of our computations.

The general recommendation when using any of the above described models is to carefully check for the validity of the hypotheses on which the model itself is based. However, in Authors' opinion, before deciding to discard a test that seems to be *suspect* in the sense of ISO 25217 one should try to look at the test results in a more general fashion and attempt anyway to get the information they contain. The underlying hypothesis is that experimental data do contain information even if noise (in the largest sense of errors, uncertainties and imperfections of any kind) is quite high, which a priori seems reasonable.

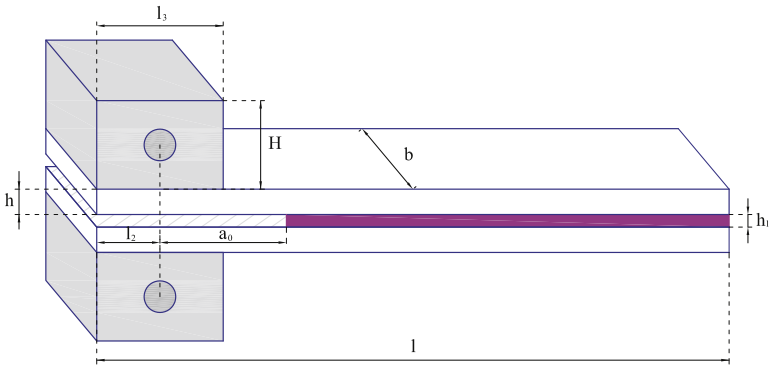

Fig. 3. DCB specimen with load blocks used in experimental tests. Geometry and dimensions.

3. Experimental and classical data reduction

Fracture tests were carried out on the symmetric DCB configuration with end load blocks depicted in Fig. 3. The specimens considered consist of two metal adherends designed to remain elastic throughout the loading process and connected by a planar thin adhesive layer where an initial pre-crack is introduced.

3.1. Material properties and specimen manufacture

The adherends made of Al 2024-T351 alloy were cut from a 1×1 m^2 plate before bonding and curing; coupons dimensions were: length l = 200.0 mm, width b = 20.0 mm or b = 25.0 mm and thickness h = 8.0 mm, see also Table 1. After cutting four holes of 4.1 mm diameter on each coupon they were connected to stainless steel load blocks using M4 screws as fasteners. Once the surface cleaned with acetone the specimens were aligned and then bonded at room temperature (25 °C) using a thixotropic, two-component epoxy with an aluminum powder filler widely used in aerospace industry (Hysol® EA 9394, produced by Henkel Corp.).

A uniform thickness of the adhesive layer of 0.190 mm was obtained by using 0.070 mm-thick copper wires at the ends of each adherend as thickness spacers plus a 0.050 mm Teflon® film that was inserted to create an initial sharp crack. Following the manufacturer datasheets, after bonding samples were cured for 3 days at room temperature to achieve normal performance. Excess adhesive on the specimen side surfaces was then removed after complete cure. The constitutive properties of the adherends and load blocks were provided by the supplier as isotropic linearly elastic with elastic modulus and Poisson's ratio of 73.0 GPa and 0.33 for aluminum and 200.0 GPa and 0.30 for steel, respectively. We emphasize that the above elastic moduli do not coincide with those used in [18] because of the different materials.

3.2. Instrumentation and data recording

Tests were carried out on a electromechanical material testing system (MTS Insight, see Fig. 4) following the guidelines given in ISO 25217. Loading and displacements were recorded with acquisition frequency of 1 Hz using a 5 kN high precision load cell, while crack progression was recorded continuously on a digital camera with 2560×1920 pixels (5 Megapixel) resolution. Markings were used on the specimen side surfaces to ease such crack tracking and crack lengths were computed manually using a linear pixel measuring toolkit (Vision Assistant, from National Instruments). During the test measurements were made over a length of 120 mm.

A small correction of the load–deflection data collected during the test was performed to account for the system compliance; this is rather standard and relatively easy to do since it basically requires a sufficiently rigid calibration specimen. Errors in the measurement of crack length, either random or systematic, are also present but more difficult to correct mainly because the exact crack tip position cannot be known but only approximately estimated to within a precision depending on the image resolution. For our purposes the crack tip was conventionally defined as the location at which the opening displacement was equal to 20 μm.

Table 1
DCB specimens geometrical parameters (dimensions in mm), see also Fig. 3.

Specimen	l	h	b	a_0	H	l_2	l_3	h_1
DCB 1x	200.	8.	25.	40.	28.	20.	40.	0.19
DCB 2x	200.	8.	20.	40.	28.	20.	40.	0.19

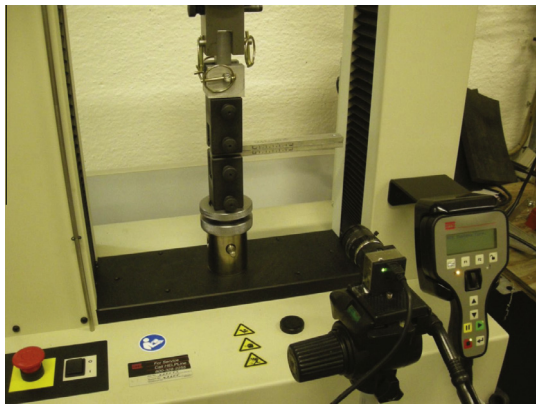

Fig. 4. DCB test configuration.

3.3. Data reduction results according to standards

Fracture tests were conducted under displacement control with a constant crosshead displacement rate of 0.1 mm/min (0.167 μm/s), that could be safely considered as a quasi-static loading. In the present study two groups of coupons of different width were prepared and a total of 14 specimen were tested in the DCB configuration (10 from series 1 and 4 from series 2). The dimensions of the two specimen series and load blocks are provided in Table 1. Each test was terminated when the crack extended for at least 50 mm beyond the initial pre-crack of length a_0. For most of them the failure mode was found to be purely cohesive fracture within the adhesive layer, see e.g. Fig. 5.

Three representative tests from series 1 and one from series 2 will be considered in the following. The test results in terms of raw load–deflection response are shown in Fig. 6.

Two issues are worth emphasizing concerning the load–deflection curves reported in Fig. 6. First is the fact that these are the raw experimental curves obtained at re-loading after the pre-cracking stage (in the sense specified in ISO 25217). Since the curves contain an initial part where take-up of plays of the loading system occurs, in the plot this part has been dropped out by resetting the displacement to zero where take-up of plays ends. This results in a non-zero value for the load (in our experiments within 10 and 30 N) at zero displacement. Second is the observation that at un-loading after pre-cracking, crack lengths for the different specimens may differ by a small amount. This contributes to originate a difference in the relevant initial loading lines and explains why the difference in elastic stiffness due to a different specimen width b is not observed in these curves. The influence of crack length a can be roughly quantified using simple beam theory. In particular, neglecting shear effects, the initial stiffness depends upon the ratio b/a^3, whereby one can check that an increase of a few percent units in the crack length suffices to mask the difference between the initial stiffness of the 20-mm and 25-mm wide specimens. Obviously, other factors such as adhesive compliance, small defects in the bondline, non-planar crack front and so forth may contribute to mask differences as well.

Besides the reduction methods described in Section 2, according to the ISO protocol the critical energy G_{Ic} has to be determined using also the Simple Beam Theory approach (SBT), which differs from CBT in that load-block and large displacement factors as well as the crack length correction are neglected. The SBT method usually gives inaccurate results since the

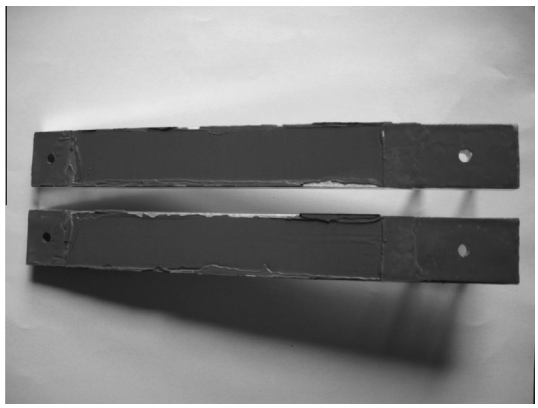

Fig. 5. Adherends surface after fracture test.

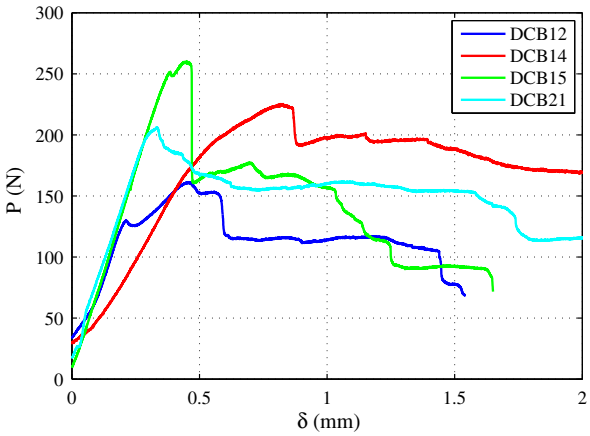

Fig. 6. Raw load-relative displacement curves for experiments DCB12, DCB14, DCB15, DCB21 at re-loading after pre-cracking.

adopted expression of the compliance is that of a rigidly built-in cantilever beam which, as in most cases, in our experiments was found to be quite far from the actual boundary condition at crack tip.

A comparison between the test results for the considered experiments is shown in Table 2. Here are reported the average values of the critical energy release rate during crack propagation computed using the different methods and the average back-calculated flexural modulus of the DCB arms defined as in [17]. Based on these average values and on ISO 25217 recommendations, the considered test results should all be qualified as *suspect*, perhaps with the only exception of DCB15, since the back-calculated elastic moduli in bending are quite different from the modulus of the aluminum substrates, see also [18].

The detail of results obtained for the DCB15 test are given in Figs. 7 and 8. In particular, the *R*-curves show that results of this test are *suspect* as well; clearly, this is as a consequence of the sudden drop-off right after the peak exhibited by the load–deflection curve and of several instabilities in the crack propagation phase.

Figs. 9 and 10 show the *R*-curves obtained using both CBT and ECM for all the considered experiments. Since the trend exhibited by these curves is different from what could be expected, in Authors' opinion a safe use of the computed values of G_{Ic} requires to take into account the reliability of the adopted reduction method and consider a suitable trendline and confidence interval. For this reason in such Figures we have also included a cubic regression and a Gaussian confidence interval with 10% exceeding probability to represent the general trend of the experimentally determined *R*-curves.

The mean values of G_{Ic} computed with the CBT and ECM are sufficiently close each other and, at least for the late propagation phase, one can reasonably establish a unique value for the fracture energy that is plotted in Figs. 9 and 10. We remind that G_{Ic} represents the specific mechanical dissipation since it is associated to the formation of a unit free surface. As such, it does not permit a complete characterization of the DCB test because it contains no information about the global amount of dissipated energy, which requires knowledge of the crack extension. In classical experimental procedures the distance ran by the crack is usually measured; a more complete characterization of the DCB test is therefore near-at-hand if a cohesive-zone model is used for carrying out data reduction.

We recall that the key difference with respect to LEFM-based models is the introduction of (at least) one additional material parameter that can be conveniently expressed either as a characteristic strength t_{max} or in the form of an interface stiffness k. This last one, together with G_{Ic}, defines the main length scale for the fracture phenomenon as:

$$l_c = \frac{E\, G_{Ic}}{t_{max}^2} \propto \frac{E}{k} \tag{11}$$

that constitutes a measure of the length over which the cohesive constitutive relation plays a role.

Various authors use similar expressions to quantify a priori the extension of the cohesive zone, see in this respect Reference [44], where is reported a table comparing different expressions proposed in the literature. In particular, one of the most widely used expressions for the size of the cohesive zone is given in [45] as

Table 2
Average values of G_{Ic} and flexural modulus E_f for the selected DCB tests computed using data reduction schemes as in References [17] and [28].

Specimen	G_{Ic} (N/mm)				E_f (GPa)
	SBT	CBT	ECM	MCCM (Ref. [28])	
DCB 12	0.034	0.032	0.041	0.062	125.008
DCB 14	0.094	0.076	0.073	0.165	169.537
DCB 15	0.048	0.050	0.054	0.087	79.083
DCB 21	0.098	0.056	0.063	0.134	211.408

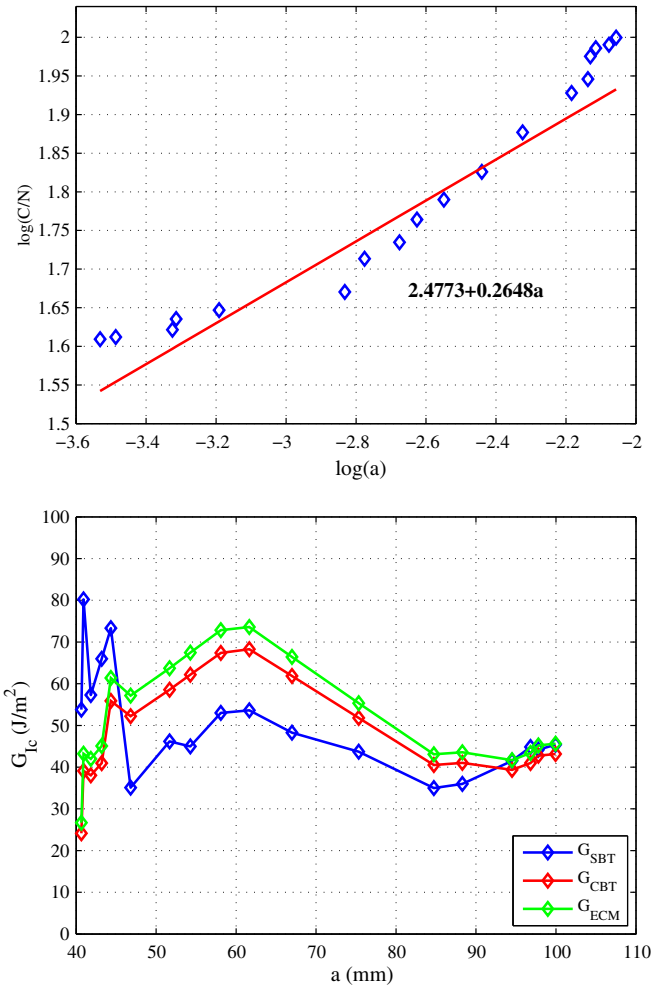

Fig. 7. Berry's regression (ECM) and *R*-curves for DCB15 test.

$$l_c = \frac{9\pi}{32}\,\frac{E}{1-\nu^2}\,\frac{G_{Ic}}{t_{max}^2} \tag{12}$$

and refers to a linearly decaying traction-separation law. Further considerations concerning length scales in the simulation of fracture and the estimation of the size of cohesive zones can be found in [26,46].

The results summarized in Table 2 show that, apart from the first test (DCB12), the average values of G_{Ic} obtained for the different specimens and with different methods are of comparable magnitude. With such values of the fracture energy a characteristic length lower than 0.1 mm, i.e. small enough to consider the LEFM hypothesis workable [27], would require an interface strength $t_{max} > 220$ N/mm^2, which is close to the yield stress of the 2024 T351 Al alloy. This seems quite unrealistic for an epoxy-bonded DCB specimen and suggests that in this case a cohesive-zone modeling is more appropriate than a LEFM-based method.

Motivated by the considerations that a complete characterization of the DCB test, and in particular of the global mechanical dissipation, requires knowledge of both size and position of the cohesive process zone, the driving rationale for our approach to identification of the cohesive parameters is to set up an inverse procedure based on one single test that uses the experimental load–deflection curve and crack extensions as data set. Actually, the fracture energy G_{Ic} controls the falling part of the load–deflection curve of the DCB, while the interface stiffness (or, equivalently, the cohesive strength) controls the translation of the cohesive process along the interface (qualitatively, the higher the stiffness, the faster the process zone moves). Moreover, a finite element model updating scheme is used that renders the present approach prone to generalization to include more general situations such as different geometries, nonlinearities in the bulk material and large displacements, with minor modifications.

Alternative to the present procedure, strength and/or stiffness of the adhesive could be obtained by performing a test directly on the bulk adhesive specimen. However, as shown in [47], bulk properties are also representative of the properties of

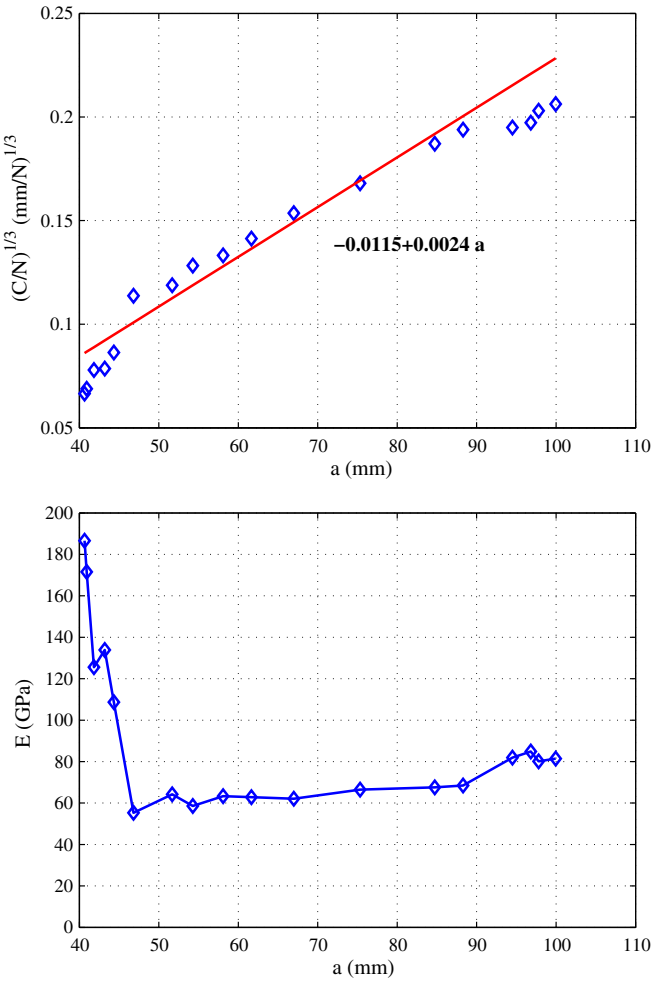

Fig. 8. Compliance regression (CBT) and back-calculated flexural modulus for DCB15 test.

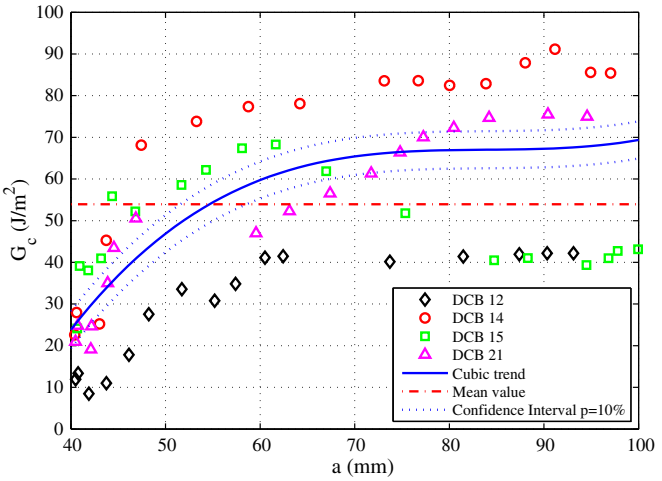

Fig. 9. Experimental *R*-curves, cubic trendlines (with 10% confidence interval) and mean values obtained using the CBT approach.

a thin adhesive layer as in a peel test or a butt joint configuration (i.e. nominally mode-I). From a practical standpoint, discrepancies always exist between results obtained considering different tests or different bondline thicknesses. Such discrep-

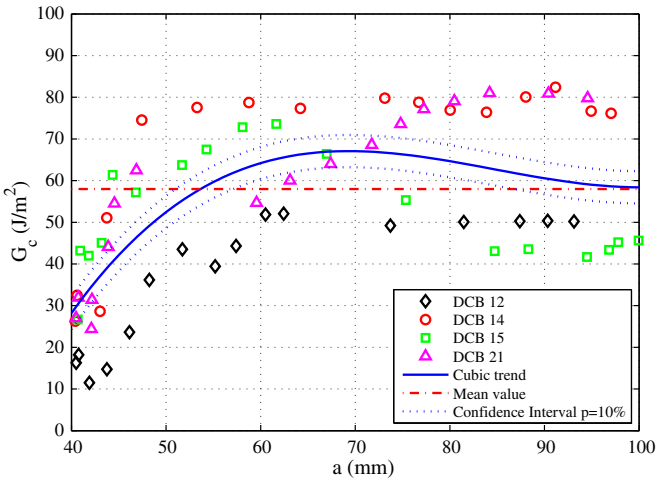

Fig. 10. Experimental *R*-curves, cubic trendlines (with 10% confidence interval) and mean values obtained using the ECM approach.

ancies do mainly originate from differences in the stress state within the adhesive layer. For instance, in thin adhesive films the apparent strength generally increases because of the almost inhibited Poisson contraction.

There are also examples of composite joints in which the apparent strength of the adhesive increases when considering a butt joint instead of a DCB geometry, see e.g. [48]. In this case the different strengths obtained for two different geometries originate from the fact that they are associated with different mechanisms, i.e. interface failure for the tensile test and primary toughening for the DCB.

In the present study the target strength parameter was the one associated with the main toughening mechanism. For this reason, focusing the analysis on one single test (the symmetric DCB) to identify the two cohesive parameters fits well to the purpose.

4. Cohesive model

In the developments that follow we refer to the interface cohesive model contributed in [39] and consider the one-dimensional mode I case. In particular, using a parametrization in terms of interface stiffness and fracture energy the state equations read:

$$\begin{aligned} t &= (1-D)k\langle[\![u]\!]\rangle_+ + k^-\langle[\![u]\!]\rangle_- \\ Y &= \frac{1}{2}k\langle[\![u]\!]\rangle_+^2 \end{aligned} \tag{13}$$

t and Y being the interface traction and the damage-driving force, $D \in [0,1]$ is the scalar damage variable, $[\![u]\!]$ is the displacement jump in the direction normal to the interface while k and k^- are the undamaged interface stiffnesses in tension and compression, respectively. The impenetrability constraint is introduced in penalty form via the stiffness coefficient k^- and by explicitly distinguishing between the positive $\langle\cdot\rangle_+$ and negative part $\langle\cdot\rangle_-$ of the displacement jump.

Irreversible damage is introduced by prescribing a bounded damage-driving force Y, a normal damage evolution and using the appropriate Karush–Kuhn–Tucker conditions:

$$\begin{aligned} &\phi = Y - Y^* \leqslant 0 \\ &\dot{Y}^* = \dot{D}\,\frac{\partial F_A}{\partial D} \\ &\phi \leqslant 0; \qquad \dot{D} \geqslant 0; \qquad \dot{D}\,\phi = 0 \end{aligned} \tag{14}$$

The critical damage-driving force Y^* is determined by a monotonically increasing positive function F_A in a way to ensure that the energy dissipated in the formation of a new unit traction-free surface equals the critical strain energy release rate G_{Ic}, namely:

$$\int_0^{+\infty} Y\dot{D}(t)\,\mathrm{d}t = G_{Ic} \tag{15}$$

In particular, the exponential traction-separation relationship presented in [39], see also Fig. 11, can be obtained using:

$$F_A(D) = -G_{Ic}\log(1-D) \tag{16}$$

An alternative parametrization of the model in terms of the interface strength t_{max} and fracture energy can be obtained by computing the peak traction as the value corresponding to the vanishing tangent stiffness, that is:

$$t_{max} = \exp(-1/2)\ \sqrt{kG_{Ic}}$$

and inverting this relationship to get the change of variables:

$$k = \exp(1)\ \frac{t_{max}^2}{G_{Ic}} \tag{17}$$

The above expression highlights one of the basic differences between the two parametrizations, i.e. that the fracture energy G_{Ic} is not completely uncorrelated with respect to the interface strength t_{max}. On the contrary, it can be shown that no correlation at all exists between G_{Ic} and the interface stiffness k, i.e.:

$$\frac{\partial\ G_{Ic}}{\partial k} = \int \frac{\partial\ t}{\partial k}\ \mathrm{d}[\![u]\!] = 0 \tag{18}$$

see also [37] for a more detailed discussion. For this reason, when plotting the results of our computations in Section 6 we shall occasionally refer to the variables G_{Ic} and k in order to use orthogonal cartesian coordinates.

In closing this section we recall that for the cohesive model described above no time-discretization is required for computing the damage state, that can be evaluated in a completely explicit way. In particular, for damage loading ($\dot{D} > 0$), at each time τ the damage variable is defined as:

$$D(\tau) = \min\left(1, \max_{(\sigma \leqslant \tau)}\left\{1 - \exp\left(\frac{-Y^*(\sigma)}{G_{Ic}}\right)\right\}\right) \tag{19}$$

The above relationship expresses the fact that damage at current time τ can be computed as the maximum over all past instants $\sigma \leqslant \tau$ of the values of damage resulting from the inversion of the expression (16).

4.1. Cohesive law linearization

In view of the application of Newton's method to solve the discretized boundary value problem as well as for the evaluation of sensitivities to be used in the identification problem, the linearized cohesive relationship is needed in the form:

$$\mathrm{d}t = K_{tan}\ \mathrm{d}[\![u]\!] \tag{20}$$

with

$$K_{tan} = \frac{\partial t}{\partial [\![u]\!]} \tag{21}$$

being the material tangent. In particular, for the case at hand the tangent is computed from (13)–(16) as:

$$K_{tan} = (1-D)k\frac{\partial \langle [\![u]\!] \rangle_+}{\partial [\![u]\!]}\left(1 - \gamma_D \frac{k\langle [\![u]\!] \rangle_+}{G_{Ic}}\right) + k^- \frac{\partial \langle [\![u]\!] \rangle_-}{\partial [\![u]\!]} \tag{22}$$

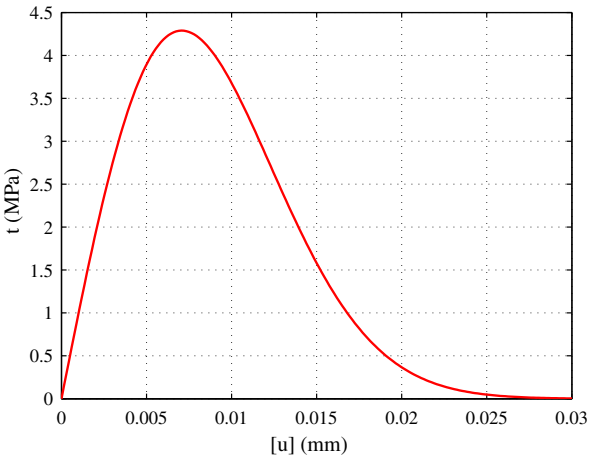

Fig. 11. Exemplificative traction–separation relationship to be identified. Depicted curve corresponds to the choice $k = 1000$ N/mm^3, $G_{Ic} = 0.05$ N/mm for the material parameters.

where γ_D is a scalar factor that equals 0 or 1 for elastic unloading and damage loading respectively, while the derivatives of the positive and negative parts of the displacement jumps read:

$$\frac{\partial\langle[\![u]\!]\rangle_{\pm}}{\partial[\![u]\!]}=\frac{1}{2}(1\pm\operatorname{sgn}([\![u]\!])) \tag{23}$$

5. FE-based identification procedure

The cohesive model defined in section 4 depends on two material parameters; for the purpose of identification via the standard DCB test we shall use the parametrization:

$$\boldsymbol{x}=\begin{bmatrix} t_{max} \\ G_{Ic} \end{bmatrix} \tag{24}$$

The optimal parameters $\hat{\boldsymbol{x}}$ will be obtained from the solution of a nonlinear programming problem in which a cost function ω expressing the gap between measured and computed quantities is minimized.

In the following we shall consider as data set for identification suitable subsets of the recorded reaction forces and of the (conventional) fracture extensions. These will be respectively collected in the vectors $\boldsymbol{P}^{meas}$ and $\mathbf{a}^{meas}$ of dimensions n_τ and m_τ, with $1,\ldots,n_\tau$ and $1,\ldots,m_\tau$ being the measurement stations, not necessarily coincident, for loads and crack extensions. The analogous quantities computed via finite element (FE) analysis will be denoted as $\boldsymbol{P}^{comp}$ and $\mathbf{a}^{comp}$.

Defining the two normalized residual vectors:

$$\mathbf{R}_P(\boldsymbol{x})=\frac{\boldsymbol{P}^{meas}-\boldsymbol{P}^{comp}(\boldsymbol{x})}{\|\boldsymbol{P}^{meas}\|} \tag{25}$$

$$\mathbf{R}_a(\boldsymbol{x})=\frac{\mathbf{a}^{meas}-\mathbf{a}^{comp}(\boldsymbol{x})}{\|\mathbf{a}^{meas}\|} \tag{26}$$

the cost function is set as:

$$\omega(\boldsymbol{x})=\alpha_P\|\mathbf{R}_P\|^2+\alpha_a\|\mathbf{R}_a\|^2 \tag{27}$$

Where the scalars $0\leqslant\alpha_P,\alpha_a\leqslant 1$ weight the two addends in order to make them comparable at the beginning of the optimization procedure. It bears emphasis that in the implemented identification scheme most of the considered data refer to the crack propagation phase. More explicitly, corrections on the initial part of the experimental load–deflection curves as described in ISO 25217 are left out since in the residuals (25) and (26) are not included the points that would be concerned by such corrections, i.e. points at the beginning of each experiment where deviations from linearity typically occur due to take-up of plays.

In the present procedure the identification problem is set up as:

$$\hat{\boldsymbol{x}}=\arg\min_{\boldsymbol{x}}\ \omega(\boldsymbol{x}) \tag{28}$$

and for its solution two methods have been employed, namely the constrained simplex algorithm, see e.g. [49], and a gradient-based Trust Region method [50], both available in the Matlab Optimization Toolbox [51]. The two optimization algorithms are well known to possess different properties. In particular, the constrained simplex is a zero-order algorithm, is very robust but its convergence rate is quite poor, while the Trust Region algorithm is first-order, convergence is generally faster and each vector $\boldsymbol{x}$ generated during the minimization sequence is strictly feasible.

Owing to the specific features of the experimental data, the Trust Region algorithm occasionally can converge to a local minimum; for this reason, in our computations the constrained simplex has been employed as a first check before using the gradient-based algorithm. However, one could alternatively find more convenient to employ the simplex algorithm only if the Trust Region converges to unrealistic values of the parameters or yields not sufficiently small residuals.

In the first-order algorithm one needs the gradients of the objective function with respect to the parameters $\boldsymbol{x}$ to be identified. As for the derivatives of the reaction forces:

$$\frac{\partial\boldsymbol{P}^{comp}}{\partial G_{Ic}};\quad\frac{\partial\boldsymbol{P}^{comp}}{\partial t_{max}} \tag{29}$$

in the present implementation they have been obtained using direct differentiation to compute the sensitivities of the finite element solution vector. This amounts to the solution of a linear problem whose right-hand side is a pseudo-load vector and the coefficient matrix is the mechanical tangent [52]. On the contrary, the derivatives of the crack extensions $\mathbf{a}^{comp}$ can be computed only indirectly. This can be achieved based on the consideration that, during fracture propagation, the amount of energy $\Phi(\tau_i)$ dissipated from the beginning of the experiment up to instant τ_i, to which corresponds a relative displacement $\delta(\tau_i)$, is:

$$\Phi(\tau_i)=\int_0^{\tau_i}P^{comp}(\xi)\cdot\delta(\xi)\ \mathrm{d}\xi-\frac{1}{2}P^{comp}(\tau_i)\cdot\delta(\tau_i) \tag{30}$$

that is, in discretized form

$$\Phi(\tau_i) = \sum_{k=1}^{i} P^{comp}_{(k)} \cdot (\delta_{(k)} - \delta_{(k-1)}) - \frac{1}{2} P^{comp}_{(i)} \cdot \delta_{(i)} \tag{31}$$

where use is made of the shorthand notation $P^{comp}_{(k)} = P^{comp}(\tau_k)$ and $\delta_{(k)} = \delta(\tau_k)$.

Relationship (30) is shown in pictorial form in Fig. 12, where the two addends can be easily recognized, i.e. the integral of the reaction force with respect the prescribed displacement and the subtractive term representing the area underneath the elastic unloading branch. Since the derivatives of the reaction forces with respect to the material parameters are known by direct differentiation, the derivative of the energy dissipated up to time τ_i with respect to parameter $\boldsymbol{x}_j$ can be computed as:

$$\frac{\partial \Phi(\tau_i)}{\partial \boldsymbol{x}_j} = \sum_{k=1}^{i} \frac{\partial P^{comp}_{(k)}}{\partial \boldsymbol{x}_j} \cdot (\delta_{(k)} - \delta_{(k-1)}) - \frac{1}{2} \frac{\partial P^{comp}_{(i)}}{\partial \boldsymbol{x}_j} \cdot \delta_{(i)} \tag{32}$$

Denoting as $a^{comp}_{(i)}$ and $\overline{G}_{Ic,(i)}$ respectively the computed crack length and average fracture energy at time τ_i, one has:

$$\overline{G}_{Ic,(i)} = \frac{\Phi(\tau_i)}{a^{comp}_{(i)}} \tag{33}$$

whereby the derivative of the crack length at instant τ_i is obtained as:

$$\frac{\partial a^{comp}_{(i)}}{\partial \boldsymbol{x}_j} = \frac{1}{\overline{G}_{Ic,(i)}} \frac{\partial \Phi(\tau_i)}{\partial \boldsymbol{x}_j} \tag{34}$$

The above expression is the one we implemented for use in the gradient-based optimization algorithm.

6. Results and discussion

Finite element computations required for the purpose of parameter identification have been carried out using a customized version of the FE code FEAP [53]. Therein has been implemented the model presented in Section 4 along with all procedures required for computing the crack progression and the gradients with respect to material parameters needed in the first-order optimization algorithm.

The FE mesh used in computations is shown in Fig. 13; it consists of 3580 4-noded Enhanced Assumed Strain elements for the bulk material and 125 2-noded interface elements for which 2-point Gauss quadrature is used. The size of interface elements in the middle of the DCB specimen is 1 mm. For values of the fracture energy as high as those computed in Section 2, such size should allow to have several elements within the process zone and resolve it adequately if the cohesive strength does not exceed the value $t_{max} = 30$ N/mm^2.

In the numerical simulation of the symmetric DCB test plane stress conditions are considered. The left end of the structure is free whilst the boundary conditions on the right part are simply supported at the centroid of the load blocks (end-rotations are allowed) with an increasing vertical displacement prescribed on the upper load block. In our computations we did not take advantage of symmetry since in these experiments we also tried to recognize the whole motion experienced by the samples (rigid-body displacements included) by comparing the results of our simulations with the pictures taken during the test to follow the crack progression.

In the following we discuss the results of identification based on the optimization procedure presented in Section 5 as well as comparisons with analogous results obtained using the data reduction schemes presented in Section 2. Four data set were considered in computations, i.e., those referred to the representative experiments whose load–deflection response

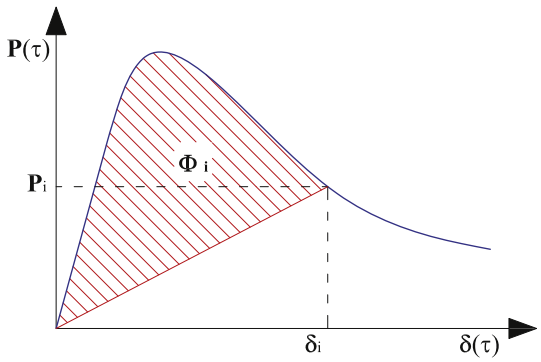

Fig. 12. Schematic of the global load-relative displacement curve and dissipated energy Φ_i at instant τ_i.

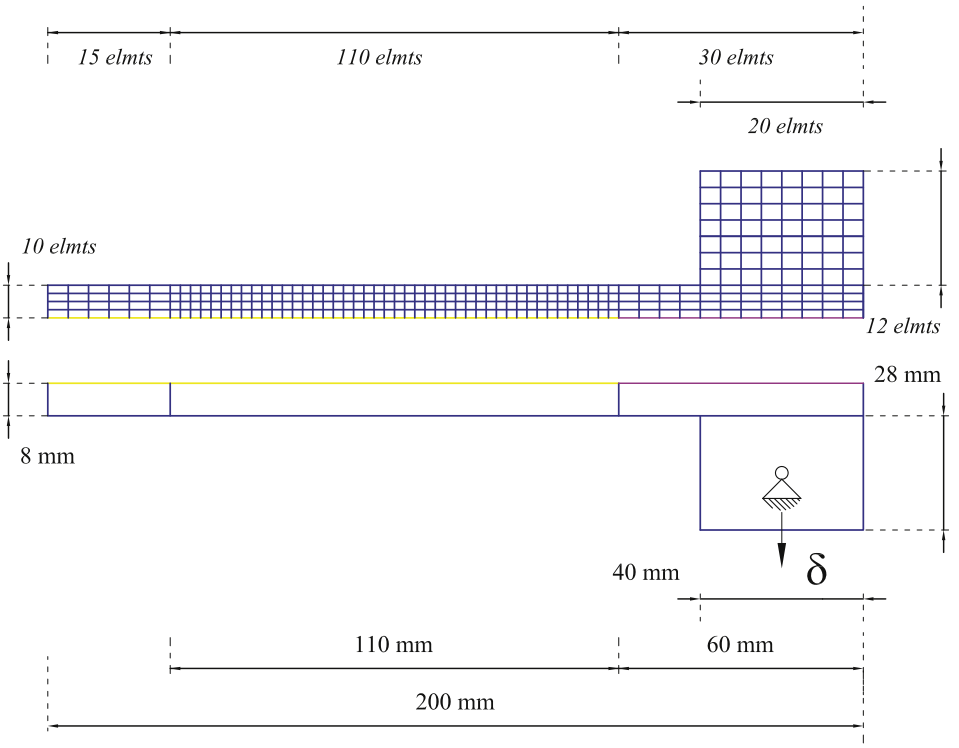

Fig. 13. DCB specimen with end load blocks. Geometry and FE mesh used for identification.

is depicted in Fig. 6. For the sake of conciseness experiments labeled DCB12 and DCB15 will not be fully documented at this stage.

For each data set the minimization of the cost function (27) was performed for two different choices of the weighting coefficients α_P and α_a. In particular, static data have always been included in the cost function taking $\alpha_P = 1$ and $\alpha_a = 0$ or $\alpha_a = 1$ have been alternatively considered to assess the influence of crack progression data on the computed material parameters. The results of our computations are summarized in Table 3. These have been obtained using as initial guess for the material parameters a unit cohesive strength t_{max} and the average values of G_{Ic} computed via ISO data reduction, see Table 2. As expected, using different weights in the cost function different results are arrived at. In particular, including the crack extension in the cost function ($\alpha_a = 1$) leads to higher values of the cohesive strength; on the contrary, the identified values of the fracture energy are nearly the same regardless of this change in the cost function.

Table 4 summarizes the average values of G_{Ic} computed using the different methods. These results show that FE-based identification provides appreciably different values (approximately 65% higher) for the fracture energy with respect to ISO data reduction and quite similar values (12% lower) compared to those obtained using MCCM, see Eq. (7). The coefficient of variation is approximately 35% in all cases, indicating that the examined tests are quite noisy and data scattering is non-negligible.

It bears emphasis that one of our arguments in favor of the proposed data reduction method is analogous to the one used to motivate use of relationship (7) in Reference [28]. Therein it is explicitly noted that when dealing with an ideal DCB specimen the energy release rate can be computed with the same accuracy regardless of the adopted formula. Whether the same robustness in identification can be achieved with noisy information is however a key point to be addressed since noise al-

Table 3
Interface material parameters identified via residual minimization.

Specimen	$\alpha_a = 0$		$\alpha_a = 1$	
	t_{max} (N/mm^2)	G_{Ic} (N/mm)	t_{max} (N/mm^2)	G_{Ic} (N/mm)
DCB 12	1.000	0.063	1.882	0.059
DCB 14	1.000	0.162	2.340	0.134
DCB 15	2.457	0.087	3.544	0.084
DCB 21	3.515	0.131	8.679	0.122

Table 4
Average values of fracture energy identified using data reduction schemes as in References [17] and [28] and FE-based optimization (proposed method).

	G_{Ic} (N/mm)		
	Average ISO	Average MCCM (Ref. [28])	Present ($\alpha_a = 1$)
DCB 12	0.036	0.062	0.059
DCB 14	0.081	0.165	0.134
DCB 15	0.051	0.087	0.084
DCB 21	0.072	0.134	0.122

ways affects truly experimental data. A discussion about this aspect has been also provided by the first Author in a previous paper, see e.g. [37].

In terms of methodology, classical data reduction procedures provide point-wise values of the fracture energy from which one has to take the average in a suitable interval; on the contrary, in the present approach a unique value of G_{Ic} is computed that minimizes the discrepancy of the numerical response with respect to the whole body of experimental data. This is not a secondary issue but, rather, a feature that strongly characterizes the identification scheme based on residual minimization.

A careful analysis of Fig. 14 reveals the distinctive feature of the present FE-based identification, i.e. that the area underneath the curve labeled *Present* coincides (to within a certain approximation) with the area underneath the experimental response, which in turn is related to the dissipated energy.

Compared to the curve labeled *ISO*, the difference in dissipated energy is approximately 30%. Hence, being the difference in terms of G_{Ic} about 65%, it follows that crack propagation is quite different in the two cases. In particular, the lengths of the crack corresponding to the last point on the graphics in Fig. 14 are about 95 mm for ISO and 75 mm for the Present (a difference of about 25%). This is also a consequence of the different elastic interface stiffness in the two cases. For instance, using relationship (17) one has a stiffness $k = 267$ N/mm^3 for ISO and $k = 163$ N/mm^3 for the Present case, which confirms that the ISO curve is accompanied by a faster crack progression.

The reasons for the differences observed above can traced back to the two important sources of error affecting the ISO identification procedures. The first, more obvious, source of error is due to inaccuracies in measurements of the crack length a, that both CBT and ECM use for the determination of G_{Ic}, see e.g. (3) and (5). In particular, due to the limited resolution of any measuring toolkit, one could expect that crack lengths are systematically underestimated. This is however not sufficient to explain all the differences between the computed responses that can be appreciated in Fig. 14. Here the experimental load–deflection curve for DCB12 is plotted against those computed using the same value of the cohesive strength ($t_{max} = 1.882$ N/mm^2) and $G_{Ic} = 0.036$ N/mm or $G_{Ic} = 0.059$ N/mm for the fracture energy, that respectively correspond to the average values obtained from ISO and FE-based identification. With such values the characteristic length parameter l_c defined in (11) is found to vary between 740 mm and 1216 mm.

As for the second source of error for G_{Ic}, it can be identified with the high compliance of the adhesive, which renders LEFM-based methods hardly applicable. The quite high values for the parameter l_c suggest that a better estimate of the fracture energy can be obtained from the Winkler-type model using (9), which however requires a priori knowledge of the interface stiffness k. To this end one may use (17) if all terms entering this expression are known. In particular, taking the values

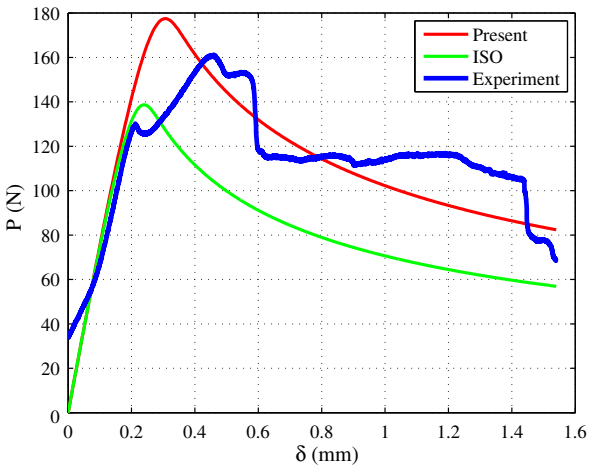

Fig. 14. DCB12 specimen. Experimental VS computed load–deflection curves. Computed curves correspond to $t_{max} = 1.882$ N/mm^2 and $G_{Ic} = 0.036$ N/mm or $G_{Ic} = 0.059$ N/mm respectively for ISO- and Present FE-based methods.

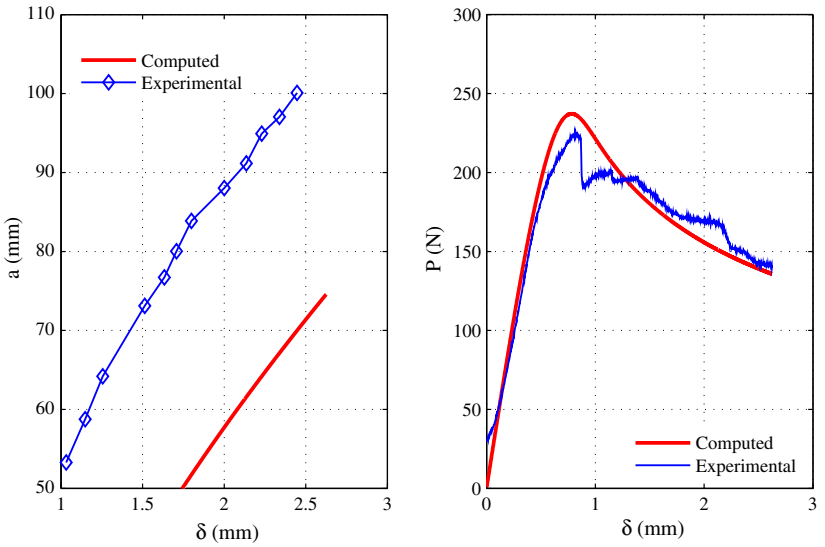

Fig. 15. DCB14 specimen. Experimental vs computed crack propagation and load-relative displacement curves. Identification without crack length ($\alpha_a = 0$). Identified parameters: $t_{max} = 1.0$ N/mm^2, $G_{Ic} = 0.162$ N/mm, $k = 16.78$ N/mm^3.

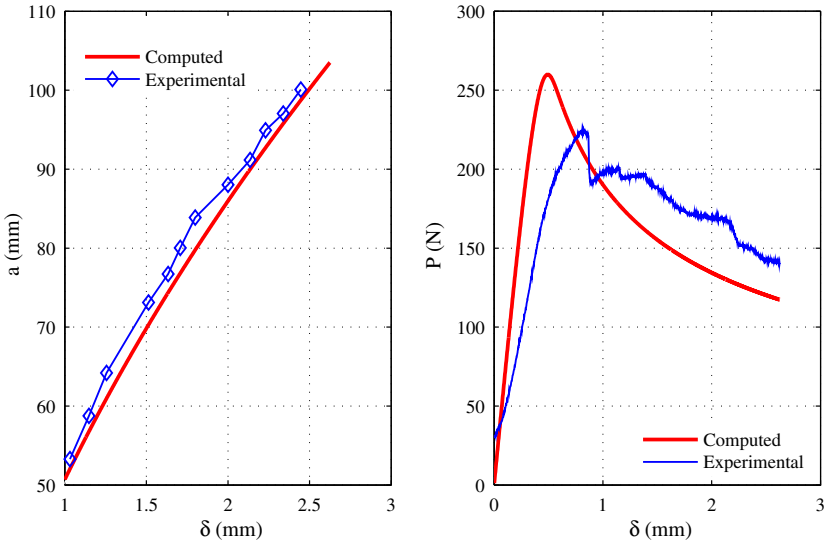

Fig. 16. DCB14 specimen. Experimental vs computed crack propagation and load-relative displacement curves. Identification with use of crack length ($\alpha_a = 1$). Identified parameters: $t_{max} = 2.340$ N/mm^2, $G_{Ic} = 0.134$ N/mm, $k = 111.08$ N/mm^3.

obtained from FE-based identification one has $k = 163$ N/mm^3, whereby $G_{Ic} = 0.057$ N/mm from (9). In absence of this information, an approximate value of the interface stiffness parameter k can however be computed requiring that for a given crack extension a the stiffness P/δ of the beam on the elastic foundation equals the experimental initial elastic stiffness. This last one can in turn be estimated via a linear regression on the first part of the load–deflection curve. For the DCB12 curve depicted in Fig. 14, where the initial crack length at re-loading after pre-cracking is $a = 43.75$ mm, the initial stiffness estimated with a linear regression between $\delta = 0$ mm and $\delta = 0.250$ mm is 465 N/mm. From (8) and (10) one then gets $k = 95$ N/mm^3, whereby the fracture energy is evaluated from (9) as $G_{Ic} = 0.062$. This last value is practically coincident with the one obtained via the FE-based identification when using $\alpha_a = 0$ in the cost function, i.e. neglecting data on the measured crack extension.

It remains now to analyze and discuss the properties of the different solutions obtained for the cohesive parameters using the FE-based identification procedure with $\alpha_a = 0$ and $\alpha_a = 1$. Based on Table 3 no major difference is expectable in the computed responses of the DCB since the values of the fracture energy in the two cases are very close each other. Changes in interface stiffness, on the contrary, are significant (about one order of magnitude), but this only influences the shape of the cohesive law. The effect of the change in stiffness could be considered to produce very limited effects based on the con-

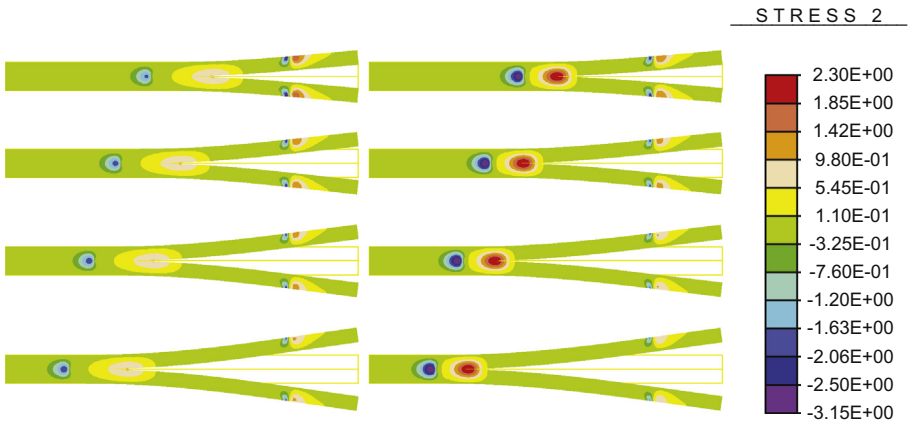

Fig. 17. DCB14 specimen. Contours of 22-stress for the two FE solutions corresponding to the material parameters computed with $\alpha_a = 0$ (left) and $\alpha_a = 1$ (right). Deformed shape is plotted with a magnification factor 10.

sideration that the falling part of the DCB load–deflection curve depends only from G_{Ic}. One can readily verify this conjecture by comparing the experimental crack propagation and load–deflection curves of DCB14 and DCB21 specimens with the curves computed from the solutions obtained using $\alpha_a = 0$ and $\alpha_a = 1$ respectively.

Figs. 15 and 16[1] refer to DCB14 specimen. In particular, plots on the left-hand side show the experimentally recorded crack progression (blue) VS the computed crack length (red) while plots on the right-hand side are the global DCB load–deflection curves. The load–deflection curve in Fig. 15 (right side) seems to show that the experiment and the simulation match pretty well. On the contrary, looking at crack progression on the left side, the experiment looks quite far from the simulation. Whether the load–deflection curve depicted in Fig. 16 constitutes an improvement with respect to the one in Fig. 15 basically depends on how much the point values of this curve are representative of the behavior of the DCB under examination.

In Authors' opinion such point values are not the most representative of the structural behavior, and this at least for two reasons. First is the fact that the experimental load–deflection curve is not as smooth as it should theoretically be, whereby trying to represent it via the closest smooth curve (in least squares sense) is not the best interpretation we can give of it. This is indeed the result reported in Fig. 15, i.e. the outcome of the minimization when the data set contains only the global experimental load–deflection curve ($\alpha_a = 0$). Second, the initial (undamaged) interface stiffness obtained from the solution of the inverse problem is in this case quite small and close to the physical lower bound for the stiffness (which has always to be positive). As shown in detail hereafter, this is likely to occur because of the particular shape of the cost function surface which may render the minimization difficult in absence of additional data that improves the quality of information. The datum that leads to a better (and more physical) solution is the crack progression that, once explicitly accounted for in the cost function ($\alpha_a = 1$), allows one to obtain the results summarized in Fig. 16.

We recall that in order to follow the crack advancement, in our measurements the crack tip is conventionally defined as the point where the opening displacement equals 20 μm. In practice, in this way we measure only increments of the crack length and do not need to know where exactly the crack tip is. Worth noticing is also the fact that computed load–deflection curves shown in Figs. 15 and 16 look different in terms of (global) peak load and initial stiffness but, as a result of the least-squares minimization, they both provide the same dissipated energy as of the experimental curve. In the Authors' opinion the dissipated energy is much more characterizing for the DCB test than the details of the global load–deflection curve, which may incorporate several kinds of uncertainties, instabilities, defects due to imperfect interface and so forth. For this reason, the information concerning the dissipated energy has been made more explicit by inserting the measurements of the crack front in the cost function, whose minimization leads to a pair of material parameters (G_{Ic}, t_{max}) that are likely to be more trustworthy.

The quite significant differences between the solutions that correspond to the two pairs of material parameters computed using $\alpha_a = 0$ and $\alpha_a = 1$ can be appreciated from Fig. 17. Here are reported the contour plots of the 22-stress (normal vertical component) on the arms of the DCB that mainly serves to put forward how different are the size of the cohesive zone and the position of the crack front in the two cases. In particular, it is noted that when explicitly accounting for the crack extension in the cost function the solution that is obtained for the cohesive parameters is stiffer, which also means that the damage process zone shrinks, see in this respect also (11). Likewise, prescribing no specific constraint on the size and position of the damage process zone, which is equivalent to setting $\alpha_a = 0$, produces a less stiff solution, which is justified by the fact that reducing the stiffness of the interface allows for an easier resolution of the damage process zone with the adopted finite element mesh. Nevertheless, in the case $\alpha_a = 0$, the inverse identification of the material parameters, and in particular of the cohesive strength, is much more difficult.

[1] For interpretation of color in 'Figs. 15 and 16', the reader is referred to the web version of this article.

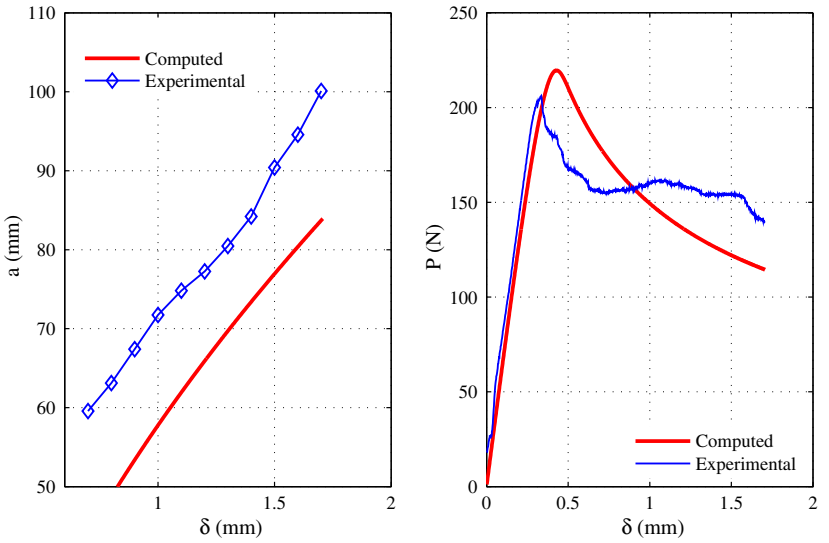

Fig. 18. DCB21 specimen. Experimental vs computed crack propagation and load-relative displacement curves. Identification without crack length ($\alpha_a = 0$). Identified parameters: $t_{max} = 3.515$ N/mm^2, $G_{Ic} = 0.131$ N/mm, $k = 256.37$ N/mm^3.

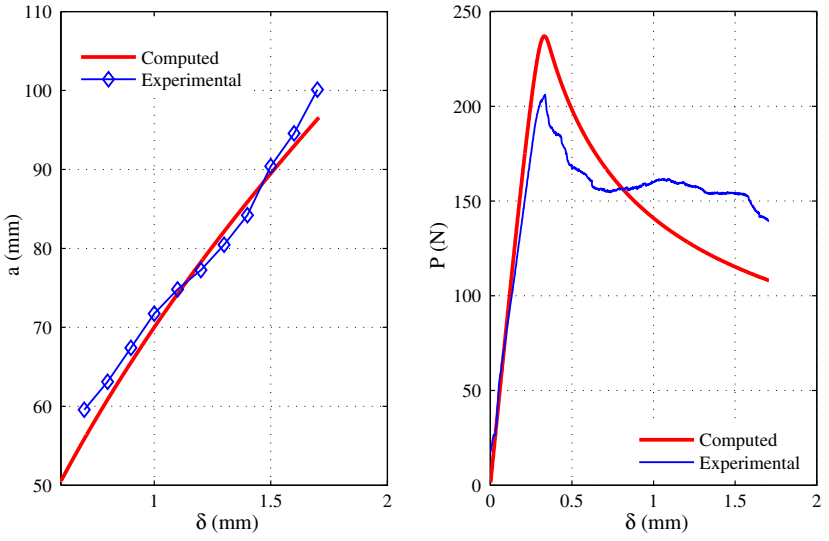

Fig. 19. DCB21 specimen. Experimental vs computed crack propagation and load-relative displacement curves. Identification with use of crack length ($\alpha_a = 1$). Identified parameters: $t_{max} = 8.679$ N/mm^2, $G_{Ic} = 0.122$ N/mm, $k = 1678.32$ N/mm^3.

This point is discussed in more detail hereafter with reference to the DCB21 specimen. At this stage we decided to refer to the DCB21 test in order to show that, in spite of the less pronounced differences between the solutions obtained for $\alpha_a = 0$ and $\alpha_a = 1$ with respect to the previous case, see e.g. Figs. 18 and 19, even for the DCB21 test there remains a fundamental difference in the cost function to be minimized.

The above referred difference is illustrated through the surface plots of the cost function depicted in the last series of plots (Figs. 20–23) that include both $\alpha_a = 0$ and $\alpha_a = 1$ cases. We emphasize in passing that in this last series of figures use has been made of the interface stiffness k as the second model parameter instead of the cohesive strength since this allows a simpler graphical representations due to the fact that the parameters k and G_{Ic} are orthogonal in the sense specified in Section 4.

Figs. 20 and 21 refer to the case $\alpha_a = 0$. The convergence path sketched on Fig. 21 shows how difficult is the minimization in this case that ends at a solution point quite close to the physical bound $k = 0$. It is also noted that the above surface plots reveal a shape of the cost function which is almost cylindrical. In particular, the surface is strictly convex with respect to the parameter G_{Ic}, which is indeed the easier parameter to identify. On the contrary, the surface is almost flat in the orthogonal direction, which makes the identification of the stiffness parameter and, by consequence, of the cohesive strength, much more difficult.

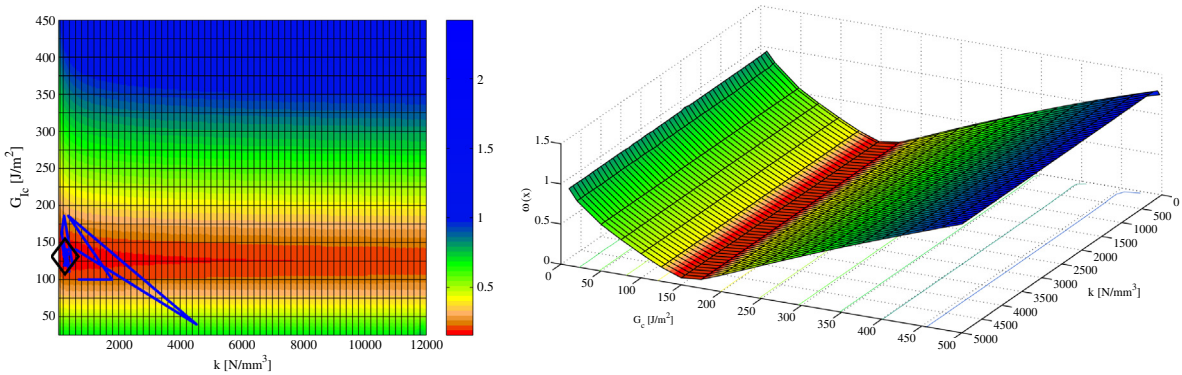

Fig. 20. DCB21 specimen. 2D (left) and 3D (right) plot of cost function with $\alpha_a = 0$.

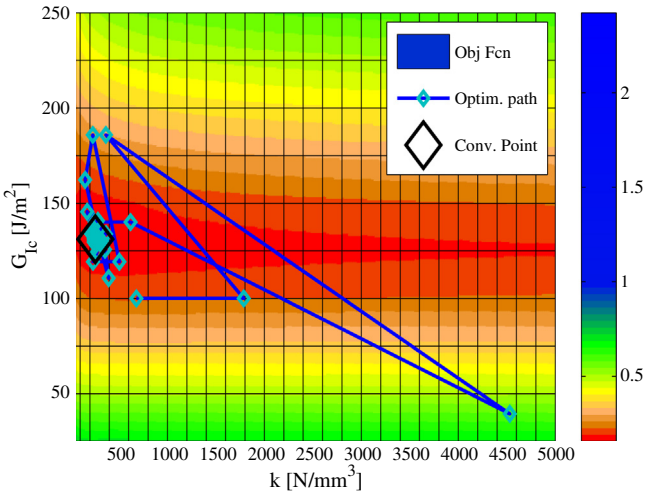

Fig. 21. DCB21 specimen. 2D plot of cost function with $\alpha_a = 0$. Enlarged view on the minimization path.

The global beneficial effect due to the introduction of the crack extension in the cost function is clearly evidenced in Figs. 22 and 23, that correspond to the case $\alpha_a = 1$. In this case, the surface shows a different shape with a global minimum that is well detectable and located sufficiently far from the physical bounds. The change in shape of the cost function surface is even more evident from the comparison of Figs. 21 and 23, which show a global convexification effect on the cost function due to the explicit introduction of the crack extension, whereby the minimization is more easily achieved.

7. Closure and future research directions

A novel approach has been presented for the identification of mode-I fracture parameters of bonded interfaces based on the DCB test. The proposed procedure has been shown to allow for the determination of both fracture energy and interface strength using one single experimental test. It makes use of the same identical data set as of ISO 25217 protocol and of a finite element model updating scheme in which a cost function expressing the normalized distance between the collected data and the computed response is minimized.

The results obtained for several experimental data sets have enlightened the crucial role played by the crack length in the solution of the identification problem. This is not very surprising since a robust identification needs a robust characterization of the problem at hand. In particular, a complete characterization of the DCB test requires knowledge of the dissipation occurring during the test that, for the case at hand, depends from both the size and the position of the cohesive zone. Actually, as shown in the paper, the extension and the motion of the process zone along the interface crucially depend upon the interface stiffness or, equivalently, the cohesive strength.

Besides the possibility of identifying two material parameters instead of the only fracture energy G_{Ic}, in the Authors' opinion the proposed methodology entails at least three more significant advantages.

First is the fact that, as shown by the examples documented in the paper, the present procedure is able to deal with situations in which the ISO procedure would fail either because of the excessive compliance of the adhesive layer or due to a behavior not sufficiently smooth to be interpreted based on a beam theory or a simplified compliance calibration method.

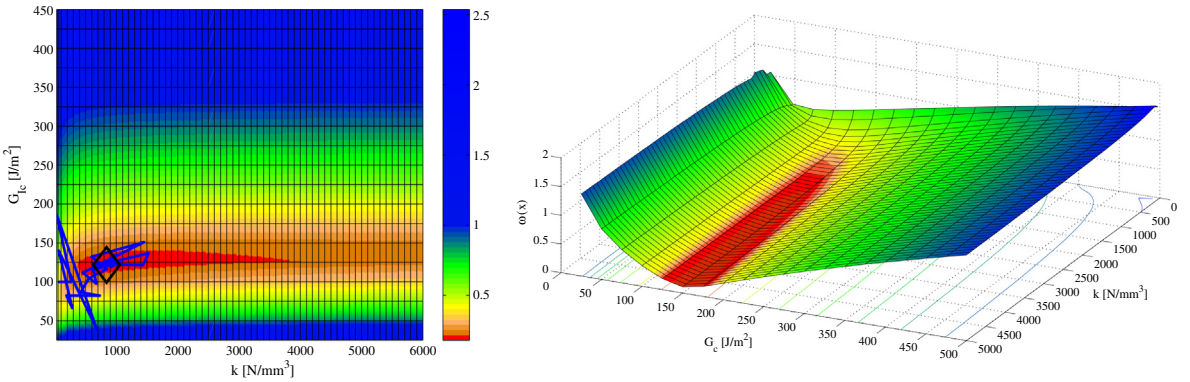

Fig. 22. DCB21 specimen. 2D (left) and 3D (right) plot of cost function with $\alpha_a = 1$.

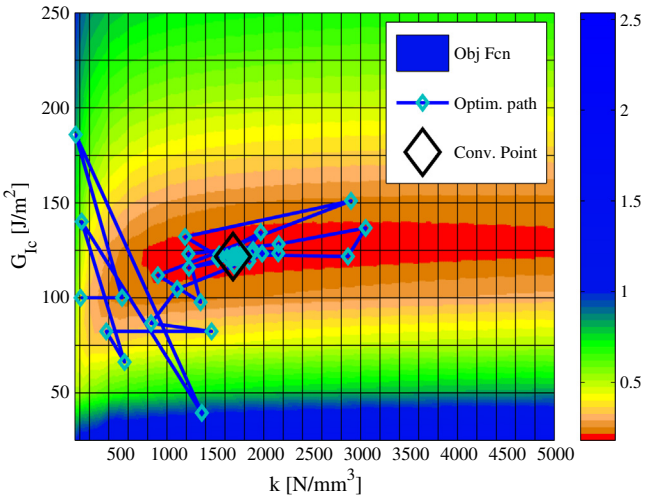

Fig. 23. DCB21 specimen. 2D plot of cost function with $\alpha_a = 1$. Enlarged view on the minimization path.

Second is the character of the proposed identification scheme, that in a sense is more immediate and objective with respect to the ISO procedure, for which a successful identification of the fracture energy is more dependent from the skillfulness of the operator and requires several qualitative considerations on the computed data as well.

A third distinctive feature of the present approach is a better coherence between the data reduction scheme and a general finite element model in which the fracture parameters and/or the cohesive laws are being used for predictive computations.

The proposed methodology is quite easy to implement and requires minor modifications for mixed-mode situations and other specimen geometries. Generalizations to accommodate nonlinear material behavior for the adherends can also be achieved with limited effort. This is particularly true for isotropic plasticity models, for which closed-form expressions of the stress update [54] and fully intrinsic return mapping algorithms [55,56] are available for computing via DMM the sensitivities that serve to obtain the gradients needed in the optimization step.

In order to effectively deal with such situations one would need to extract more detailed and sophisticated information from the fracture tests such as those provided by full-field measurements via Digital Image Correlation procedures [57]. In this perspective, deformation of the adherends in the plastic range is expected to improve the quality of the experimental data with respect to the elastic case data because plasticity is likely to reduce the noise-to-signal ratio.

In view of their relevance for applications, these last topics deserve further research work and will be addressed in forthcoming papers.

Acknowledgements

This research has been partly carried within the project *Analysis of structural adhesive joints. Modeling and experimental testing* within the MiSE-ICE-CRUI 2008 research program. The financial support of the Italian Ministry of Economic Development (MiSE) and the Italian Institute for Foreign Trade (ICE) are gratefully acknowledged. Authors also wish to thank the Anonymous Reviewers for all useful remarks and comments that definitely contributed to improve the quality of the paper.

References

[1] Adams RD. Adhesive bonding: science, technology and applications. Boca Raton: CRC Press; 2005.
[2] Klarbring A, Movchan AB. Asymptotic modelling of adhesive joints. Mech Mater 1998;28(14):137–45.
[3] Lebon F, Rizzoni R, Ronel-Idrissi S. Asymptotic analysis of some nonlinear soft thin layers. Comput Struct 2004;82(2326):1929–38 [Computational Structures Technology].
[4] Schmidt P, Edlund U. Analysis of adhesively bonded joints: a finite element method and a material model with damage. Int J Numer Methods Engng 2006;66(8):1271–308.
[5] Lebon F, Rizzoni R. Asymptotic behavior of a hard thin linear elastic interphase: an energy approach. Int J Solids Struct 2011;48(34):441–9.
[6] Rizzoni R, Lebon F. Asymptotic analysis of an adhesive joint with mismatch strain. Eur J Mech – A/Solids 2012;36(1):1–8.
[7] Frémond M. Adhérence des solides. Journal de Mécanique Théorique et Appliquée 1987;6(3):383–407.
[8] Raous M, Cangémi L, Cocu M. A consistent model coupling adhesion, friction, and unilateral contact. Comput Methods Appl Mech Engng 1999;177(34):383–99.
[9] Talon C, Curnier A. A model of adhesion coupled to contact and friction. Eur J Mech – A/Solids 2003;22(4):545–65.
[10] Del Piero G, Raous M. A unified model for adhesive interfaces with damage, viscosity, and friction. Eur J Mech – A/Solids 2010;29(4):496–507.
[11] Johnson KL, Kendall K, Roberts AD. Surface energy and the contact of elastic solids. Proc Roy Soc Lond. A. Math Phys Sci 1971;324:301–13.
[12] Maugis D. Contact, adhesion and rupture of elastic solids. Heidelberg: Springer Verlag; 2000.
[13] Dugdale DS. Yielding of steel sheets containing slits. J Mech Phys Solids 1960;8(2):100–4.
[14] Barenblatt GI. The mathematical theory of equilibrium cracks in brittle fracture. Adv Appl Mech 1962;7:55–129 [Elsevier].
[15] Xie D, Waas AM. Discrete cohesive zone model for mixed-mode fracture using finite element analysis. Engng Fract Mech 2006;73(13):1783–96.
[16] Sun CT, Jin Z-H. Chapter 9 – cohesive zone model. In: Fracture mechanics. Boston: Academic Press; 2012. p. 227–46.
[17] International Organization for Standardization. ISO 25217. Adhesives – determination of the mode I fracture energy of structural adhesive joints using double cantilever beam and tapered double cantilever beam specimens. Technical report, Geneva (Switzerland); 2009.
[18] Blackman BRK, Kinloch AJ, Paraschi M, Teo WS. Measuring the mode I adhesive fracture energy, G_{IC}, of structural adhesive joints: the results of an international round-robin. Int J Adhes Adhes 2003;23(4):293–305.
[19] Hashemi S, Kinloch AJ, Williams JG. The analysis of interlaminar fracture in uniaxial fibre–polymer composites. Proc Roy Soc Lond. A. Math Phys Sci 1990;427(1872):173–99.
[20] Blackman B, Dear JP, Kinloch AJ, Osiyemi S. The calculation of adhesive fracture energies from double-cantilever beam test specimens. J Mater Sci Lett 1991;10:253–6. 10.1007/BF00735649.
[21] Berry JP. Some kinetic considerations of the Griffith criterion for fracture II: Equations of motion at constant deformation. J Mech Phys Solids 1960;8(3):207–16.
[22] Shokrieh MM, Heidari-Rarani M, Ayatollahi MR. Interlaminar fracture toughness of unidirectional DCB specimens: a novel theoretical approach. Polym Test 2012;31(1):68–75.
[23] Song SJ, Waas AM. Mode i failure of laminated polymeric composites. Engng Fract Mech 1994;49(1):17–27.
[24] Song SJ, Waas AM. Energy-based mechanical model for mixed mode failure of laminated composites. AIAA J 1995;33(4):739–45.
[25] Hillerborg A, Modéer M, Petersson P-E. Analysis of crack formation and crack growth in concrete by means of fracture mechanics and finite elements. Cem Conc Res 1976;6(6):773–81.
[26] Falk ML, Needleman A, Rice JR. A critical evaluation of cohesive zone models of dynamic fracture. J Phys IV, Proc 2001;11(5):43–50 [Special Issue].
[27] Li S, Wang J, Thouless MD. The effects of shear on delamination in layered materials. J Mech Phys Solids 2004;52(1):193–214.
[28] Tamuzs V, Tarasovs S, Vilks U. Delamination properties of translaminar-reinforced composites. Compos Sci Technol 2003;63(10):1423–31.
[29] de Moura MFSF, Morais JJL, Dourado N. A new data reduction scheme for mode I wood fracture characterization using the double cantilever beam test. Engng Fract Mech 2008;75(13):3852–65.
[30] Suo Z, Bao G, Fan B. Delamination *R*-curve phenomena due to damage. J Mech Phys Solids 1992;40(1):1–16.
[31] Andersson T, Stigh U. The stress-elongation relation for an adhesive layer loaded in peel using equilibrium of energetic forces. Int J Solids Struct 2004;41(2):413–34.
[32] Nilsson F. A tentative method for determination of cohesive zone properties in soft materials. Int J Fract 2005;136:133–42. 10.1007/s10704-005-5125-y.
[33] Kim H-G, Chew HB, Kim K-S. Inverse extraction of cohesive zone laws by field projection method using numerical auxiliary fields. Int J Numer Methods Engng 2012;91(5):516–30.
[34] Sørensen BF, Brethe P, Skov-Hansen P. Controlled crack growth in ceramics: the DCB specimen loaded with pure moments. J Eur Ceram Soc 1996;16(9):1021–5.
[35] Sørensen BF, Jacobsen TK. Determination of cohesive laws by the J-integral approach. Engng Fract Mech 2003;70(14):1841–58 [Cohesive Models].
[36] Gustafson PA, Waas AM. The influence of adhesive constitutive parameters in cohesive zone finite element models of adhesively bonded joints. Int J Solids Struct 2009;46(10):2201–15 [Special Issue in Honor of Professor Liviu Librescu].
[37] Valoroso N, Fedele R. Characterization of a cohesive-zone model describing damage and de-cohesion at bonded interfaces. sensitivity analysis and mode-I parameter identification. Int J Solids Struct 2010;47(13):1666–77.
[38] Fedele R, Sessa S, Valoroso N. Image correlation-based identification of fracture parameters for structural adhesives. Technische Mechanik 2012;32(2):195–204.
[39] Valoroso N, Champaney L. A damage-mechanics-based approach for modelling decohesion in adhesively bonded assemblies. Engng Fract Mech 2006;73(18):2774–801.
[40] Irwin GR. Onset of fast crack propagation in high strength steel and aluminium alloys. Sagamore Res Conf Proc 1956;2:289–305.
[41] American Society for Testing and Materials. ASTM D5528-01 (2007)-e3. Standard test method for mode I interlaminar fracture toughness of unidirectional fiber-reinforced polymer matrix composites. Technical report, Philadelphia (US); 2007.
[42] Budzik M, Jumel J, Imielinska K, Shanahan MER. Effect of adhesive compliance in the assessment of soft adhesives with the wedge test. J Adhes Sci Technol 2011;25(1–3):131–49.
[43] Jumel J, Budzik MK, Shanahan MER. Beam on elastic foundation with anticlastic curvature: application to analysis of mode I fracture tests. Engng Fract Mech 2011;78(18):3253–69.
[44] Turon A, Dávila CG, Camanho PP, Costa J. An engineering solution for mesh size effects in the simulation of delamination using cohesive zone models. Engng Fract Mech 2007;74(10):1665–82.
[45] Rice JR. The mechanics of earthquake rupture. In: Dziewonski AM, Boschi E, editors. Physics of the earth's interior. Italian Physical Society and North-Holland Publishing Co.; 1980. p. 555–649. [in: Proceedings of International School of Physics 'Enrico Fermi', Course 78, 1979].
[46] Harper PW, Hallett SR. Cohesive zone length in numerical simulations of composite delamination. Engng Fract Mech 2008;75(16):4774–92.
[47] Burst N, Adams D, Gascoigne H. Investigating the thin-film versus bulk material properties of structural adhesives. J Adhes 2011;87(1):72–92.
[48] Li S, Thouless MD, Waas AM, Schroeder JA, Zavattieri PD. Use of mode-I cohesive-zone models to describe the fracture of an adhesively-bonded polymer–matrix composite. Compos Sci Technol 2005;65(2):281–93.
[49] Byrd RH, Hribar ME, Nocedal J. An interior point algorithm for large-scale nonlinear programming. SIAM J Optim 1999;9(4):877–900.
[50] Coleman T, Li Y. An interior trust region approach for nonlinear minimization subject to bounds. SIAM J Optim 1996;6(2):418–45.
[51] The MathWorks Inc. Matlab 7.8 – optimization toolbox 4.2 Manual; 2009.
[52] Kleiber M, Hien TD, Antúnez H, Kowalczyk P. Parameter sensitivity in nonlinear mechanics: theory and finite element computations. Chichester: John Wiley; 1997.

[53] Taylor RL. FEAP – programmer manual. University of California at Berkekey; 2009. <http://www.ce.berkeley.edu/_∼rlt>.
[54] Alfano G, Rosati L, Valoroso N. A displacement-like finite element model for J2 elastoplasticity: variational formulation and finite-step solution. Comput Methods Appl Mech Engng 1998;155(3–4):325–58.
[55] Valoroso N, Rosati L. Consistent derivation of the constitutive algorithm for plane stress isotropic plasticity. Part I: Theoretical formulation. Int J Solids Struct 2009;46(1):74–91.
[56] Valoroso N, Rosati L. Consistent derivation of the constitutive algorithm for plane stress isotropic plasticity. Part II: Computational issues. Int J Solids Struct 2009;46(1):92–124.
[57] Sutton MA, Orteu J-J, Schreier HW. Image correlation for shape, motion and deformation measurements – basic concepts, theory and applications. Springer; 2009.